Journal of Applied Fluid Mechanics, Vol. 16, No. 7, pp. 1386-1401, 2023.
Available online at www.jafmonline.net, ISSN 1735-3572, EISSN 1735-3645.
https://doi.org/10.47176/jafm.16.07.1669

A Comparative Study of Film Cooling with Combined Impingement and Film Cooling

R. K. Panda[1], A. K. Pujari[2†] and B. Gudla[2]

[1] *Indian Institute of Technology, Madras, Chennai, Tamilnadu,600036, India*
[2.] *Indian Institute of Petroleum and Energy, Visakhapatnam, 530003, India*

†Corresponding Author Email: arun.pujarimec@iipe.ac.in

(Received November 22, 2022; accepted March 13, 2023)

ABSTRACT

In order to cool the gas turbine vane or blade and raise the operating temperature, two standard convective cooling methods are used: jet impingement cooling and film cooling. The current study uses computational analysis to analyze and compare film cooling effectiveness with and without multi-jet impingement cooling on a flat plate. Ansys Fluent software is used to perform computational analysis on a flat plate. The computational results were compared with the experimental result using K–ω SST turbulence model and validated with literature data. The flat plate is used for the conjugate heat transfer study on the hot surface (named interaction surface), cold surface (called target surface), and inside the film hole. Different heat transfer parameters such as heat flux, Nusselt's number, and effectiveness are compared for the two cases, i.e., film cooling with impinging jets (IFC) and film cooling without impingement cooling (FC). It is observed that the FC case shows lower effectiveness as compared to the IFC case. The average Nusselt number for the IFC cases is almost three times larger than FC. The film exit temperature values are higher FC case, but it is more uniform in the IFC case. Interaction surface heat flux and Nusselt number values show higher values on the upstream wall of the film hole for IFC than in the FC case.

Keywords: Jet impingement cooling; Film cooling; Combined impingement film cooling; Turbulent kinetic energy; Nusselt's number.

NOMENCLATURE

d	film hole diameter
D	diameter of impingement hole
h	coefficient of heat transfer
H	jet to plate distance
k	coefficient of thermal conductivity
L	plate's length
M	blowing ratio
Nuj	target surface's Nusselt number due to jet
Num	Nusselt number's mainstream
p	pitch-
P	pressure,
q"	heat flux
Rej	Reynolds number of jet
Rem	Reynolds number of mainstream
T	temperature
t	plate thickness
Voe	exit jet velocity of the orifice
u, v, w	x, y and z direction component's velocities
x, y, z	streamwise, transverse and vertical distance, respectively
y+	dimensionless wall distance
θ	dimensionless temperature

Subscript

amb	ambient
c	coolant
f	fluid
m	mainstream
oe	orifice exit
s	solid
w	wall

Greek Symbol

μ	dynamic viscosity
ν	kinematic viscosity
ρ	density
κ	turbulent kinetic energy
ω	specific dissipation rate
ε	effectiveness

1. INTRODUCTION

Gas turbine blades' internal and external sides are cooled by techniques such as impingement cooling, film cooling, pin-fin cooling, and rib-turbulated cooling. Impingement cooling maximizes localized heat transfer by impinging fluid on a hot surface. In contrast, in film cooling, effused cool air generates a thin insulating blanket over the turbine blade to reduce heat load.

Hollworth and Dagan (1980) reported average convective heat transfer from a plate that had been perforated to release the spent air from an impinging jet. They experimented with inline and staggered arrangements of holes and concluded that the inline arrays had significantly reduced heat transfer rates compared to the staggered design.

According to Metzger and Bunker (1990), heat transfer is primarily determined by the jet Reynolds number, with only marginal effects from the flow extraction rate. Results show that leading-edge metal temperatures can vary significantly due to small shifts in the alignment of the impingement nozzles throughout the span concerning the location of the film cooling holes.

As noted by Ekkad *et al.* (1999), film extraction lessens the cross-flow impact and boosts the jet impingement heat transfer. The Nusselt number between the jets grows faster when the flow migrates towards the effusion holes than the cross-flow. In addition, they saw that the exit flow orientation affected the heat transfer pattern on the target surface differently.

When an array of impinging jets is used without effusion holes, the spent air of the injected jets generates a cross-flow within the confined space and strongly affects the jet flow farther downstream, as observed by Rhee *et al.* (2003). However, the effusion holes on the target surface aid in halting the spent air's tendency to flow perpendicularly. With effusion holes, heat transfer coefficients are uniform because of the powerful impacts of cross-flow and re-entrainments of spent air. However, the effusion hole layout provides more even temperatures and higher heat transmission coefficients. Noting that "no prior research has comprehensively addressed both internal impingement cooling and external film cooling using a numerical technique," the authors state that they are the first to do so.

Miao and Wu (2006) set out to learn more about the implications of the hole's shape and the blowing ratio for a hybrid impingement/film cooling system. They discovered that the impingement leads to a lower jetting flow in the coolant tube, leading to greater efficiency than isolated film cooling.

Researchers Oh *et al.* (2008) found that the efficiency of a combined impingement and film cooling configuration would rise with an increase in the blowing ratio by conducting tests on a stainless steel flat plate and reporting that the enhancement of impingement and film cooling would grow as the blowing ratio increased, it was determined that the blowing ratio would affect the enhancement of impingement and film cooling. In addition, they reported how jet-to-plate spacing would affect film cooling and found that it would not make a difference by more than 3%. They discovered that the slight fluctuation was due to the high length-to-diameter-to-diameter ratio of the film hole used.

One jet impinging on a rib roughened flat surface was experimentally studied by Katti and Prabhu (2008). Multiple rib designs were tested, and the local heat transfer distributions were compared to those of a smooth surface. An increase in Reynold's number resulted in more significant average Nusslet numbers for rib designs compared to smooth surfaces. The greater the distance between the jet and the plate, the less efficient the heat transmission.

A higher blowing ratio and closer center-to-center spacing between neighboring holes were proposed to improve the overall cooling efficiency by Jingzhou *et al.* (2009). As effusion holes are so effective at attracting secondary flow, an impingement in the design significantly increased heat transmission. The streamwise flow was associated with decreased temperature gradient between the surface and the fluid. Heat flux was higher on the mainstream side of the effusion plate's surface than it was on the coolant side.

By using a polycarbonate plate and changing the hole configuration and gap distance for both inline and staggered designs, Jung *et al.* (2010) broadened the area of the analysis. It was found that the staggered design's effectiveness values were more consistent than those from the linear arrangement. It was found the same thing with different jet-to-plate spacing. They reasoned, nevertheless, that the higher coolant temperature wouldn't matter because of the enhanced heat transfer in the inner surface. They have eluded this to the conjugate effects in a roundabout way.

Ravelli *et al.* (2010) demonstrate that impingement cooling somewhat boosts total efficiency. Conjugate effects, such as lessening convective cooling within the coolant holes due to impingement cooling, accounted for this marginal decrease in overall effectiveness.

Raj (2013) explored coolant mainstream interactions in simultaneous impingement and film cooling and examined the flow structure at various blowing ratios. In addition, they noted that the SST-k-ω model outperformed the regular k-ω model in forecasting the temperature distribution. An indication of jet takeoff is the attachment of nodal points in the transverse plane to flow fields at the film hole's leading edge. An increase in the blowing ratio causes a more terrific lift-off, which boosts the efficiency of the holes' leading edges.

The effects of impingement hole diameter on overall cooling efficiency and heat transmission on both sides

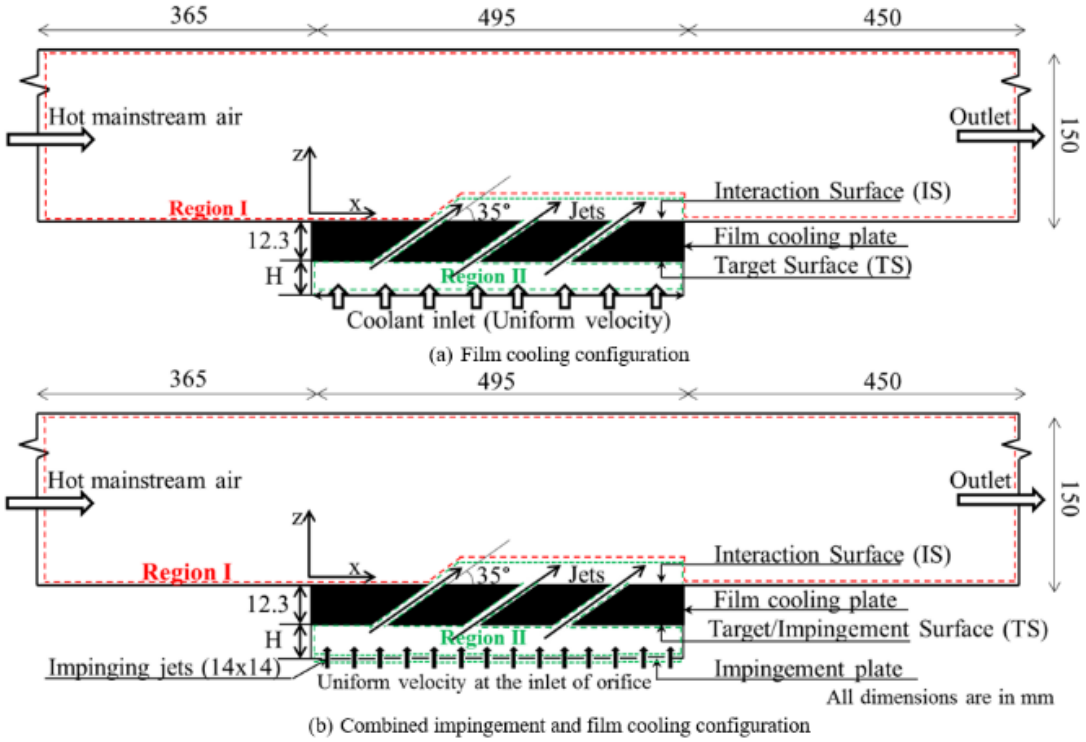

Fig. 1. Schematic diagram showing the computational domain.

of the film cooling plate were investigated by Fu *et al.* (2020). Modifying the hole's diameter was a roundabout way to affect the H/D ratio. The convective heat transfer coefficient and the impingement Reynolds number at the target surface decrease as the hole diameter increases since th e jet's velocity is decreased and its shape is changed more easily. For this reason, the impact of impingement on overall effectiveness is mitigated for large hole diameters for a given mass flow rate of the coolant.

Circular blocks on a flat plate were the subject of numerical explorations by Zhang and Wang (2019). They have determined the best placement for the films by analyzing the impact of hole sizes in the film at different places along the stream.

The effects of an upstream wake on the flow's aerodynamics and heat transmission were investigated by Babu and Anish (2020). They have performed an investigation looking at how different angles of ejection flow affect the overall velocity profile. They demonstrated that a smaller ejection angle results in more efficient film cooling.

Staggered film holes with normal and inclined-to-cooled surfaces have been studied for their impact on heat transfer by Zhang and Zhu (2021). They discovered that the jets remained close to the wall because vortices generated from injection normal to the surface. The production of vortices accelerated with an increase in the blowing ratio.

The elimination of kidney vortex was the focus of research conducted by Jiang *et al.* (2021), who examined the impact of various film cooling hole geometries and configurations. Their research found that a strong kidney-shaped vortex forms outside the film cooling hole at a high blowing ratio, resulting in inefficient cooling.

The above literature survey shows the complexity of flow and heat transfer phenomena associated with impingement and film cooling. A systematic comparison of the flow and heat transfer parameters for the film cooling (FC) configuration and the combined impingement and film cooling (IFC) configuration under conjugate thermal conditions are not available in the literature. Further, it is observed that, in conjugate studies, only film (external) cooling or impingement cooling has been investigated with little emphasis to flow within the film. The heat transfer rate depends on flow and heat transfer characteristics within the film. This study will simulate the film cooling process with and without the impinging jets and their impact on inside the cylindrical film cooling holes.

2. PROBLEM FORMULATION AND NUMERICAL METHODOLOGY

The computational domains that correspond to the physical models that were employed in the testing are illustrated in Figs 1(a) and (b), respectively.

Table 1 Geometric details of the computational domain

Dimension	Value
Diameter of impingement hole (D), mm	5.25
Diameter of film hole (d), mm	5.0
Jet-to-plate spacing ratio (H/D), mm	0.4, 1.2 and 2.0
Length of film/impingement hole plate (L), mm	495
The thickness of the impingement hole plate	4
The thickness of the film hole plate	12.3
The inclination of impingement hole to surface	90°
The inclination of film hole to surface	35°
Arrangement of film holes	3 rows and 6 columns
Arrangement of impingement holes	14 ×14 matrix
Film cooling plate cross-section	495mm × 375mm
Impingement jet plate cross-section	495mm × 375mm
Thermal conductivity of film hole plate; A, B, and C	0.2, 1.5, and 15 W/m K
Mainstream channel cross-section	375mm in height, 150 in width, and 1310mm in length

Thedomain can be broken down into three distinct sections: the first section is the hot mainstream passage, the second section is the coolant flow path, and the third section is the solid plate with a film hole. The hot mainstream air travels through the test portion at the same speed, temperature, and pressure as it enters and leaves under the same conditions. Temperature and inlet velocity is regulated consistently right at the point when the impingement plate makes contact with the air. The impingement chamber is sealed on all sides, so the coolant's only escape route is through the cylindrical film holes. The coolant escapes through the film's perforations and enters into interaction surface with the mainstream.

The following conservation equations are used for simulation and turbulence equations to solve the conjugate heat transfer problem.

Continuity Equation:

$$\frac{D\rho}{Dt} + \rho\nabla.\vec{V}=0 \tag{1}$$

Momentum Equation:

$$\rho\left(\frac{\partial\vec{V}}{\partial t} + \vec{V}.\nabla\vec{V}\right) = -\nabla p + \mu\nabla^2\vec{V} + \rho g \tag{2}$$

Energy Equation:

$$\rho\frac{D}{Dt}\left(e + \frac{\vec{V}^2}{2}\right) = p\dot{q} - \frac{\partial(up)}{\partial x} - \frac{\partial(vp)}{\partial y} - \frac{\partial(wp)}{\partial z} + \rho\vec{f}.\vec{V} \tag{3}$$

2.1 Solution Methodology

To solve the governing equations using appropriate boundary conditions, the commercial finite volume-based software program known as Ansys Fluent was used. The SIMPLE algorithm is utilized so that pressure and velocity can be coupled. For the calculation of pressure, a conventional interpolation method is used. The second-order upwind scheme is utilized for the analysis of momentum and energy. In contrast, the first-order upwind technique calculates turbulent kinetic energy and specific dissipation rate. When the highest residual value for continuity is on the order of 10^{-4} and when it is in the order of 10^{-6} for the equations of momentum, turbulence, and energy, respectively, then it is assumed that a solution is obtained.

has converged. In addition, the contact surface area-weighted average temperature is continuously

measured. Until the temperature of the cooled plate has reached a stable state, all of the computations are carried out.

A multi-block mesh has been constructed to carry out the GCI study. Hexahedral and tetrahedral mesh elements were used for creating the mesh. Denser meshes are utilized in the vicinity of the holes and the solid surfaces. The validation case uses similar meshing procedures, and the present investigation is carried out only after the results have been validated using data from the accessible literature. Figure 2 presents the three-dimensional computational models that were utilized in the simulations of the already existing physical configurations. The present model is symmetric about the plane that is depicted in Fig. 2. Table 1 contains an exhaustive listing of the information regarding the computational domain's geometrical dimensions in the numerical simulation.

At the mainstream and coolant fluid intake, experimental mass flow rate, temperature, and turbulence intensity are applied.

The computational model's boundary conditions are based on experimental data. The temperature differential between coolant and mainstream is 15K or 318K for mainstream and 303K for coolant. For IFC, the impingement hole exit Reynolds number is 825. The average grid-generated turbulence intensity at mainstream and coolant inlets is 0.9 to 1.1%. The turbulent length scale is 10% of the hydrodynamic

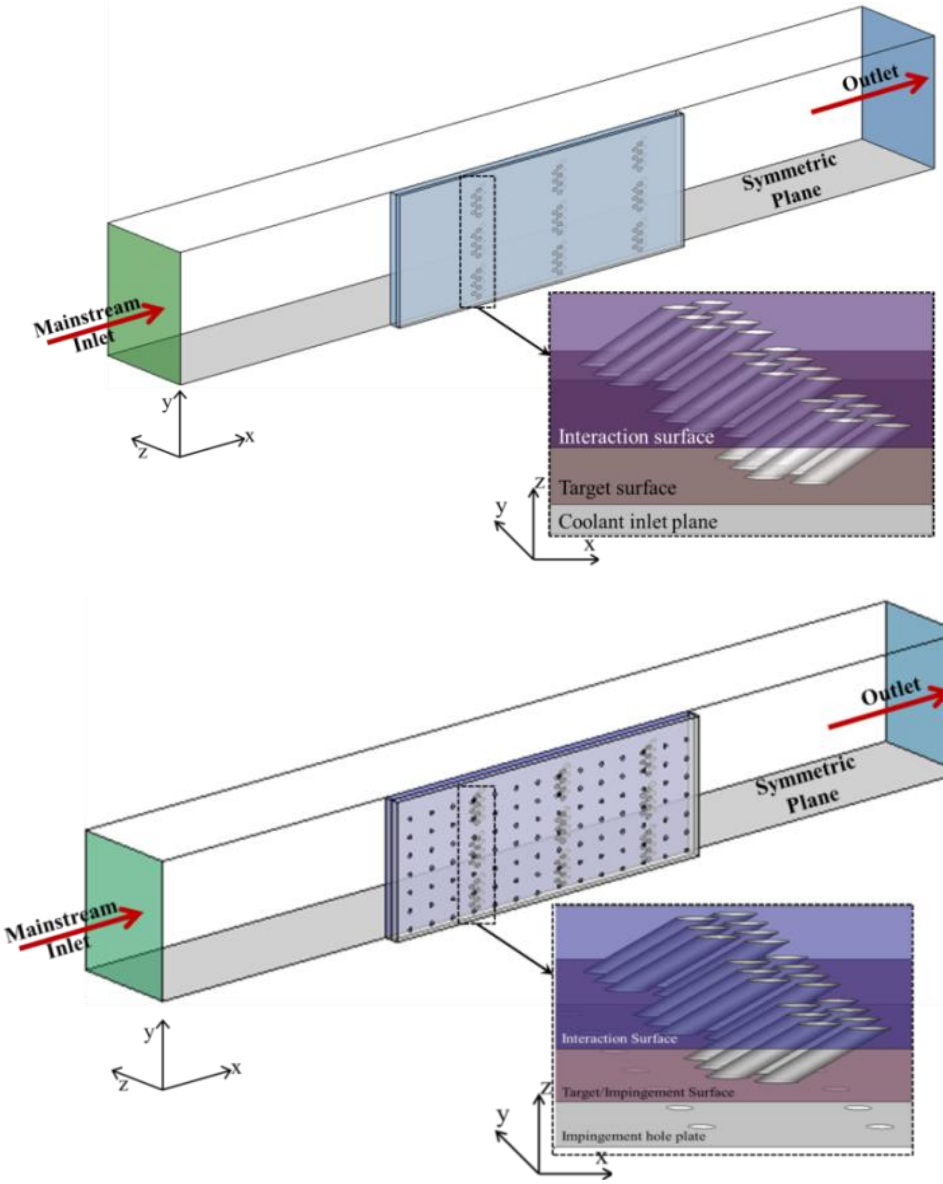

Fig. 2. Computational domain of (a) FC and (b) IFC case.

diameter at the mainstream intake border, whereas it is the impingement hole diameter at the coolant inlet. The turbulent viscosity ratio (μt/μ) is held constant at 10. Typical values for these boundary conditions are given in Table 2.

2.2 Meshing

2.2.1 Meshing Techniques

Finite volume method is used for computing the mesh. The IFC setup mesh is depicted in Fig. 3. The mesh is generated using a multi-block approach, which frees up the grid generation process and minimizes the amount of core memory needed for the computation.

Since the grids for various parts of the flow domain can be generated independently using the multi-block technique, the blocks can be connected through their inter-block boundaries. The borders between blocks in a multi-block computing domain have no physical significance. When meshing, a hybrid mesh is employed, which consists of both hexahedral and tetrahedral elements. A hexahedral mesh is used within the primary flow direction, while a boundary layer mesh is employed close to the contact surface. At a distance of 0.01 mm, the first grid dot can be seen. A tetrahedral mesh is used for the rest of the domain, which includes the cooling chamber and the film hole plate. The interaction surface features an excellent fine mesh. For the turbulence model (kω-SST) being

Table 2 Typical boundary condition

Boundary conditions	Values
Coolant inlet velocity at the orifice exit, IFC case (m/s)	1.6
Jet Reynolds number	825
Diameter of the orifice, in mm	5.25
Turbulence intensity at the orifice exit	1%
Coolant inlet velocity to plenum chamber, FC case (m/s)	0.036
Hydraulic Diameter at the coolant inlet, FC case (mm)	42.6
Coolant inlet temperature (K)	303
Mainstream turbulence intensity	1%
Mainstream inlet velocity (m/s)	1.7, 2.7, and 4.5 for M = 1.6, 1.0, and 1.6, respectively
Mainstream Reynolds number	49050, 78500, and 130800 for M = 1.6, 1.0, and 1.6 respectively
The temperature of coolant at inlet (K)	318
Turbulence intensity at the mainstream inlet	1%
Mainstream inlet hydraulic diameter (mm)	32.1
Turbulent viscosity ratio (μt/μ)	10
Gauge pressure, Pa at outlets	Zero
Temperature, K at outlets	298

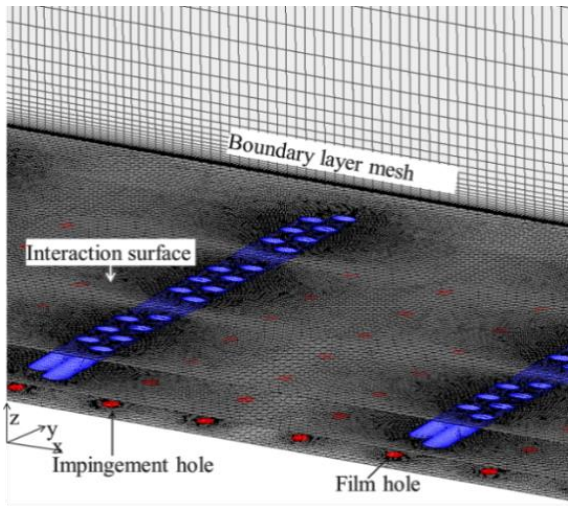

Fig. 3. Interior mesh used for computation.

Table 3 Grid used for meshing

Configuration			Coarse	Medium	Fine
IFC	H/D 1.2	N*	4.5	5.3	5.8
		y+	1.8	1.3	0.8
FC	H/D 1.2	N*	4.1	4.9	5.4
		y+	1.9	1.3	0.9

*N values are in millions

utilized in this study, a y+ value of less than 2 is considered to locate the initial cell near the wall. According to the sources we consulted, the "Grid Convergence Index" (GCI) technique is used to conduct the sensitivity analysis of the grid. The grid details used for meshing are given in Table 3. The letters in bold are the chosen grid corresponding to the model, where N is the number of cells.

2.2.2 Data Reduction

In Fig. 4, the data reduction lines and planes are shown. Multiple vertical lines (z-direction) are chosen at different streamwise locations, viz., U1, U2, and U3 at the trailing edge of 1st, 2nd, and 3rd row of film holes; L1, L2, and L3 at 0.1 times the film hole diameter (d) downstream of the 1st, 2nd and 3rd row of film holes; L11, L12, and L13 at 2.0d, 10d and 18d downstream of the first row of holes;

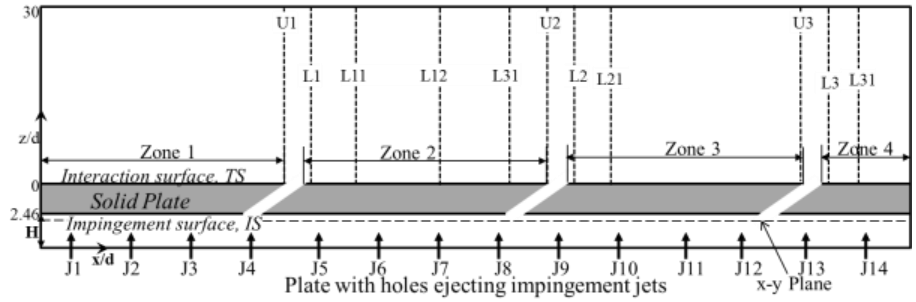

(a) x-z plane

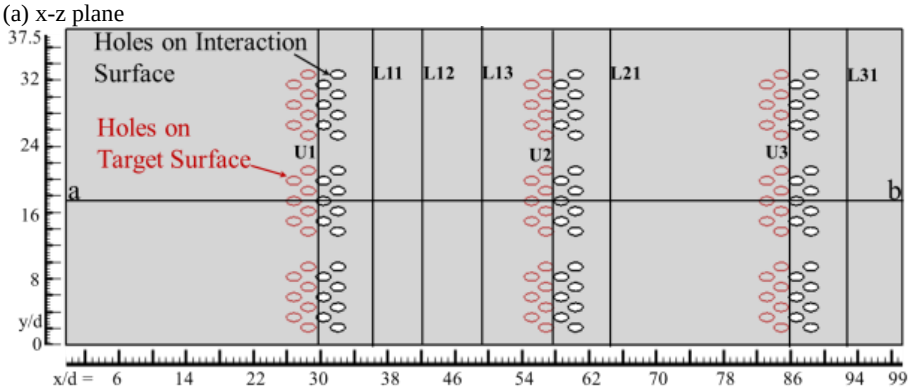

(b) x-y plane interaction and target surface

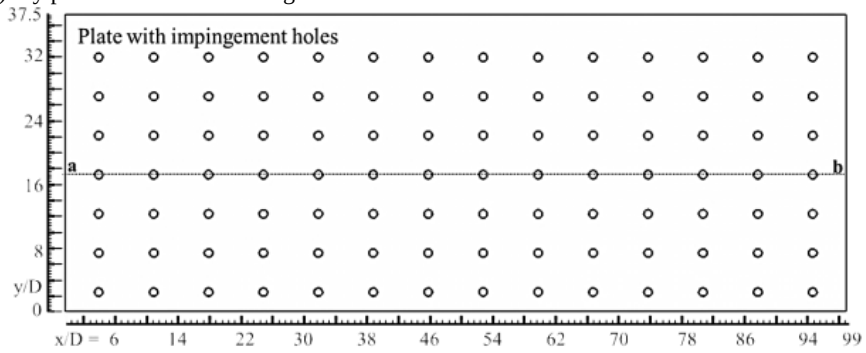

(c) x-y plane impingement surface

Fig. 4. Data reduction planes and lines.

and L21 (a). Transverse planes (y-z plane) are named after the vertical line placements above. To understand the flow pattern inside the plenum chamber (dotted line in Fig. 4), a plane (xy-plane) is considered 0.2d below the target surface (a). The plate is divided into four zones: zone 1, zone 2, zone 3, and zone 4. Zone 1 covers the entirety of the plate; zone 2 covers the downstream end of the first row of film holes; zone 3 covers the downstream end of the second row of film holes; and zone 4 covers the downstream end of the third row of film holes. Figure 5 shows the notation to avoid confusion when discussing the results. Figure 5 demonstrates the terminology used for film cooling nomenclature.

2.3 Validation

The computational methodology must be validated against a benchmark problem analogous to the issue at hand. The published experimental work of Jung *et al.* (2010) has been chosen to validate the computed results. The physical configuration, geometrical details, and input conditions are used to resolve the problem of Jung *et al.* (2010) with the currently suggested methodology and codes. A geometric model is created, and the multi-block mesh is generated using commercial software. Both hexahedral and tetrahedral mesh is employed to grid the entire domain.

For computational study, various turbulence models are utilised to compare with the experimental results of Jung *et al* (2010). In terms of centerline effectiveness for M = 0.3, 0.5, and 0.7, the κ-ω- SST model compares well to the literature. Figures 6 demonstrate the good agreement between the centerline effectiveness statistics from Jung *et al*. (2010) for M = 0.3, 0.5, and 0.7 and those derived by the κ-ω-SST model in the current investigation. The figure shows film cooling effectiveness distribution considering (Left) and without considering the film hole exit temperature (Right), where the maximum centerline effectiveness divergence is approximately 8%.

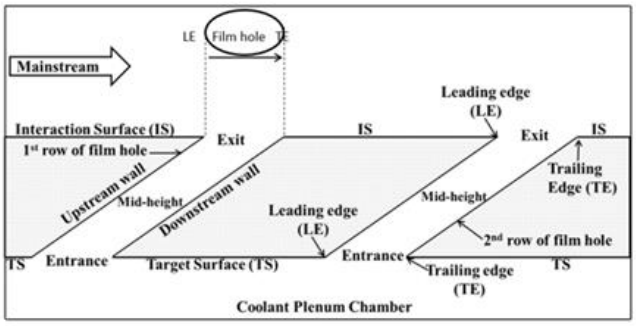

Fig. 5. Nomenclature used in film holes.

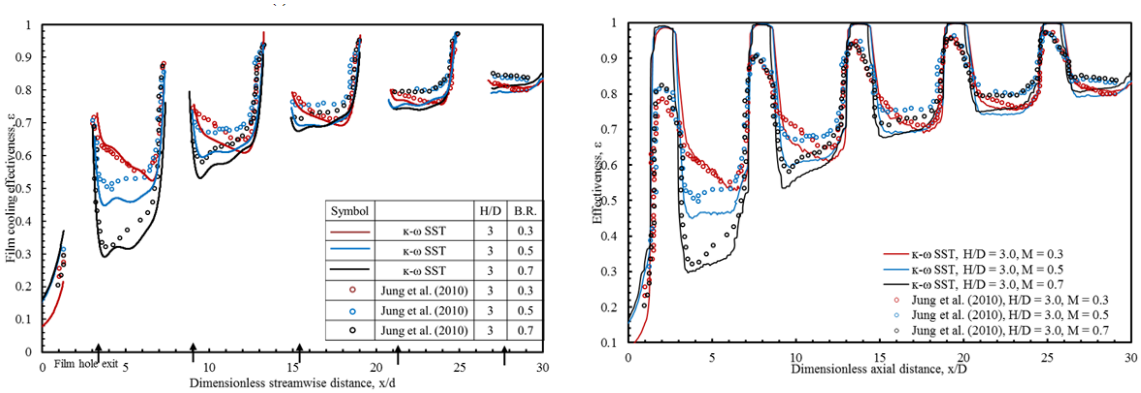

Fig. 6. Comparison of computational data with experimental data of Jung et al. (2010) with (Left) and without film hole exit temperature (Right).

The limitations of turbulence models illustrate the difference mentioned above is within the acceptable limit, as the RANS model is used for prediction in the present computation. Hence among the used turbulence models, the k-ω SST model is considered. In light of the observations above, the following results are provided using the κ-ω - SST model.

3. RESULTS AND DISCUSSIONS:

This paper presents results showing heat transfer features as well as cooling effectiveness and discusses

FC and IFC configurations. The variation of conjugate heat transfer characteristics for FC and IFC configurations near the impingement plate, inside the film holes, and in the various interacting zones of mainstream and the film coolant are discussed.

3.1 Target Surface

3.1.1 Heat Flux Variation

The axial variation of the dimensionless heat flow on the target surface is shown in Figure 7 along (line ab). The magnitude of the averaged heat flow in each zone falls somewhat from zone 1 to zone 4. This is true because the hot mainline serves as the source for the convective and conductive thermal resistances that transmit heat to the impinging fluid. The contact surface in zone 1 does not experience film cooling since it is directly exposed to the main flow, which leads to a better heat flux value at the target surface. Convective resistance increases downstream of the first row of film holes because of the presence of the coolant film between the mainstream and the plate. This is so that a barrier between the two can be created by the coolant film. Conjugate heat transfer, on the other hand, only causes a modest reduction in the axial direction heat flux. In contrast, the magnitude of the heat flow that moves through each zone in FC and IFC configurations is very different from one another. The heat flux values for the FC case are modest and almost consistently the same across all zones. On the other hand, several peaks and valleys are seen for the IFC configuration in the heat flow graphs in Figure 7. The peaks correspond to the stagnation spots, and the dips show locations between the two stagnation zones. At the stagnation point of jet 4, which impinges very near the film hole entry, the value of the heat flux is at its maximum. Even though jet 8 only partially hits the surface, it affects the hole entry, nevertheless creating a peak in the heat flux. However, the value of the heat flux produced by jet 12 is the lowest of the three. This jet completely covers the surface of the target. The interactions between the jets and the subsequent production of vortices and cross-flow are what are responsible for the observed heat flux patterns.

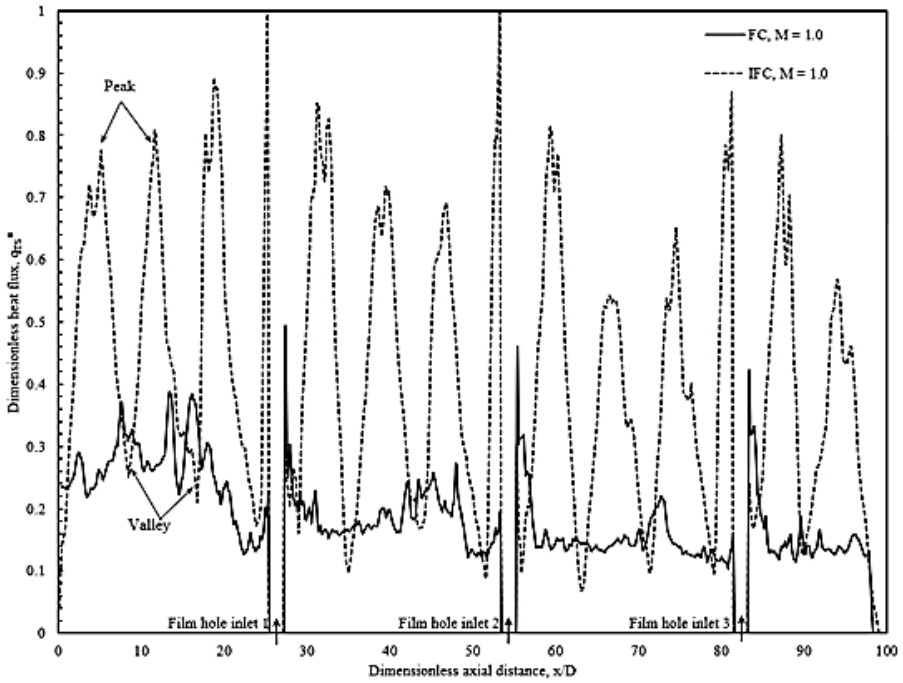

Fig. 7. Dimensionless heat flux distribution on the impingment surface along line ab for FC and IFC case.

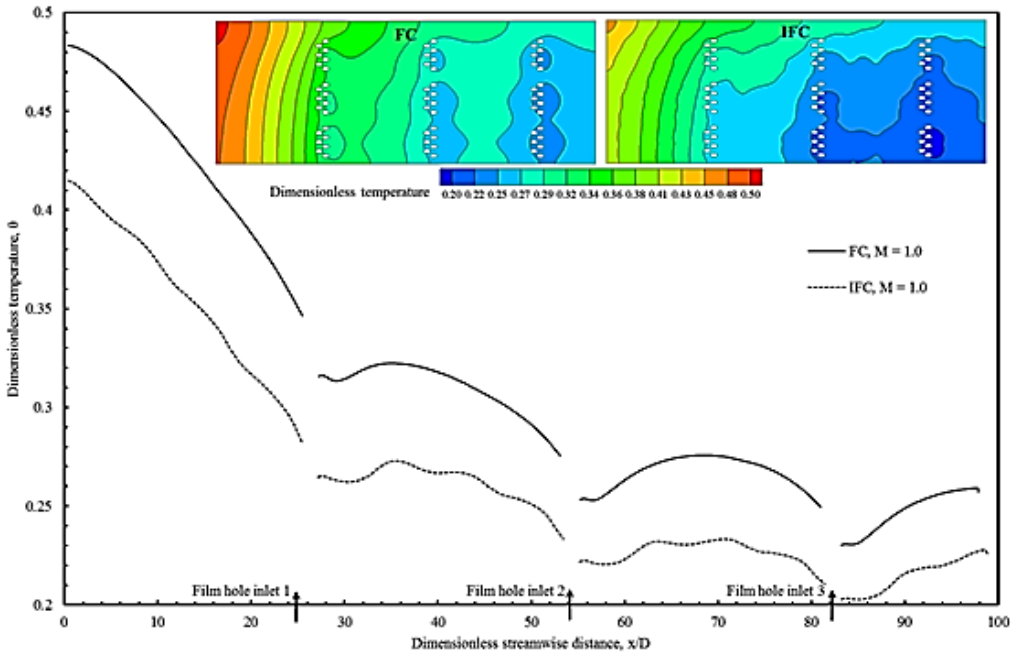

Fig. 8. Dimensionless temperature distribution for FC and IFC along the streamwise distance.

3.1.2 Temperature Variation

The dimensionless temperature distribution along line *ab* is shown in Fig. 8. The general trend of the impingement surface temperature variation is that it decreases in the downstream direction. In zone 1, the temperature value reduces rapidly for both FC and IFC cases, with higher temperatures for the former. The FC case's temperature curve is relatively smooth, but minor fluctuations are noticed in the IFC case due to jet impingement. In zone 2, the temperature value increases a little from the downstream of the film hole and then continuously decreases up to the 2nd row of film holes. In zone 3, the temperature rises from the film hole up to the mid-length of the zone and then decreases till the 3rd row of the film hole. Unlike in other zones, zone 4 temperature values rise with downstream distance until the plate's end. These variations in temperature distributions are attributed to the multiple jet interaction and coolant flow direction. Above

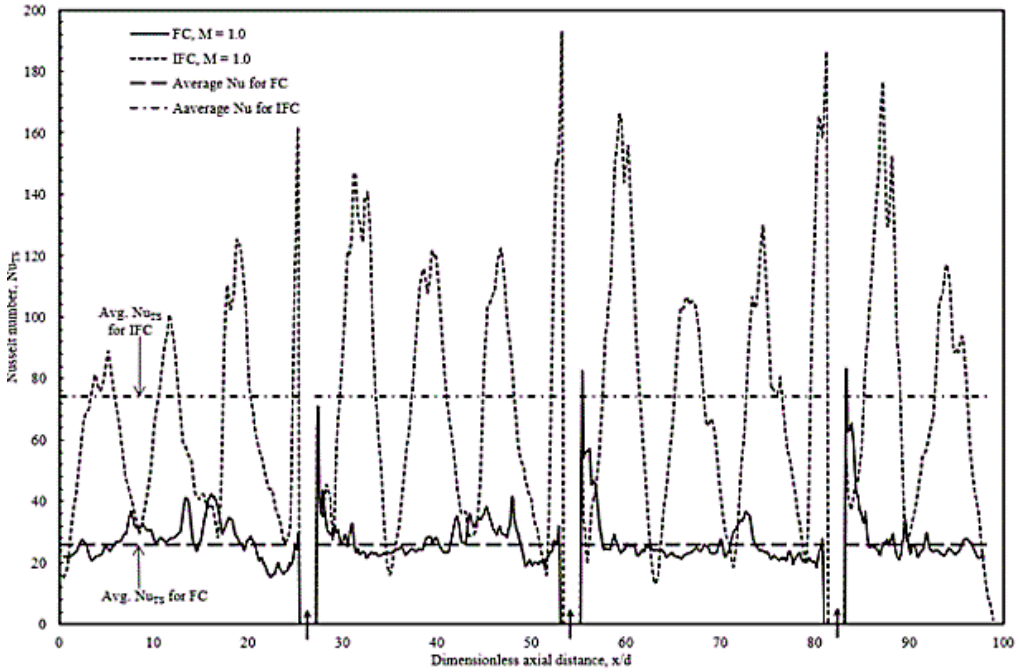

Fig. 9. Nusselt number distribution along streamwise distance for FC and IF.

mentioned temperature variation in different zones remains more or less the same for both FC and IFC cases; therefore not discussed individually. The temperature values are lower for the IFC case compared to the FC case all along the line *ab*. A variation of 17.3% in peak temperature is observed between the IFC and FC. The temperature differences between FC and IFC remain almost the same on the entire impingement surface (rear side of the plate), as shown in the insets of Fig. 8.

3.1.3 Nusselt Number Variation

The Nusselt number distributions in Fig. 9, shown along line *ab* on the impingement surface (TS), reveal the vital difference between the two configurations, even as the inlet flow and temperature at the coolant inlet are maintained the same. Due to multiple jet interactions on the IFC, the flow phenomena result in significant Nusselt number peaks on the target surface (TS). These peaks occurred at the impingement/stagnation points, which vary concerning the position of the jets. The complicated flow phenomenon inside the plenum chamber, which includes multiple jet interaction, cross-flow jet interaction, vortex generation, etc., is responsible for these variances. On the other hand, for the FC case, the average Nusselt number is negligible and remains almost constant on the surface. Only close to the film hole values are high due to flow acceleration. The average Nusselt number ratio on the target surface of the IFC and FC cases is about three times. The conjugate heat transfer properties on the interaction surface between the FC and IFC designs are undoubtedly influenced by such a significant difference. On average, there is an increase of 200% in Nu number for IFC compared to FC for Target surface.

3.2 Film Hole

3.2.1 Heat Flux Variation

Figure 10 shows the heat flux variation along the film hole's upstream (AA') and downstream (BB') walls. The variations are somewhat different between the FC and IFC case. For the FC case, along the line AA' (upstream wall), the heat flux value continuously increases from the inlet (A) till near the exit (A') of the film hole. For the IFC case**,** the maximum heat flux value is seen at the film hole's inlet (A, or the LE of the entry), and it subsequently decreases until the hole's exit. The heat flux values of FC are significantly smaller than IFC. Along the downstream side (BB') For the FC case, the heat flux decreases up to 80% of the total length of the film hole and then increases till the exit of the film hole. For the IFC case, the heat flux increases till the mid-height of the film hole and then reduces up to the exit, where it again increases. The average heat flux value along BB' for FC and IFC are close to each other. At film holes 2 and 3, the heat flux distribution along AA' and BB' remains almost the same as at film holes 1. However, the difference in magnitude progressively reduces between FC and IFC along the line AA'. On the downstream side along the line, BB, the heat flux value for the FC case remains more or less the same, but for the IFC case, the heat flux value continuously reduces, leading to the reduction in heat flux difference between FC and IFC configurations in the downstream rows. Figure 11 shows the streamlines colored with temperature in the plenum and the entrance of film hole 1 for both FC and IFC cases. The temperature pattern remains almost the same at the entrance of film holes 2 and 3, but the magnitude reduces for the film holes downstream. At the mid-height of the film hole, the temperature distribution becomes relatively uniform

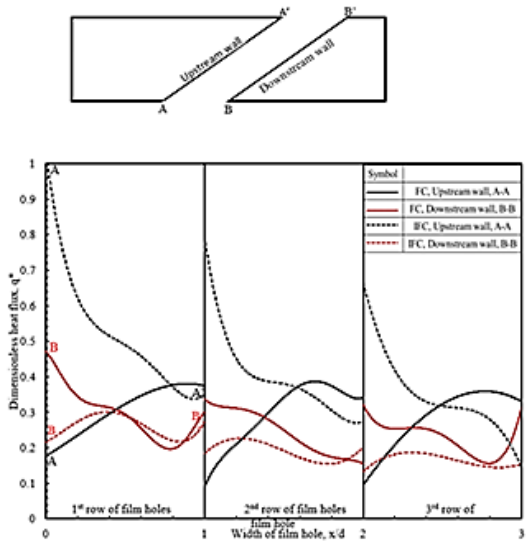

Fig. 10. Heat flux variation along the upstream (AA') and downstream (BB') wall of the film hole.

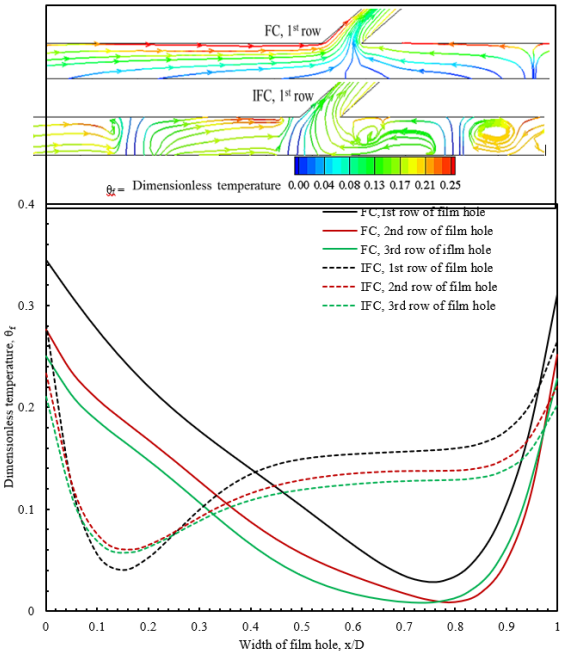

Fig. 11. Dimensionless temperature in the film hole for FC and IFC at inlet.

compared to the entrance for both FC and IFC cases. For the FC case, where the temperature value reduces from the upstream wall to the mid-height and then increases up to the downstream wall, as shown in Fig. 12. For the IFC case, the temperature value remains almost constant in most of the film hole, with an exception at the upstream and downstream walls, where the temperature increases. Insets in Fig. 12 show the contour of temperature variation inside film hole 1. The temperature distribution repeats itself in the downstream rows with a progressive reduction in the temperature magnitude.

The coolant's exit dimensionless temperature profiles are shown in Fig. 13. The magnitude and trend of the exit temperature differ noticeably between the FC and IFC systems. For the FC compared to the IFC, the temperature values along the leading and trailing edges are higher. However, they are lower in the middle of the exit section for FC. It is therefore obvious that the IFC case's temperature profile is more consistent. Similar distributions are noticed in the 2nd and 3rd rows of film holes, but with a lower range of temperature.

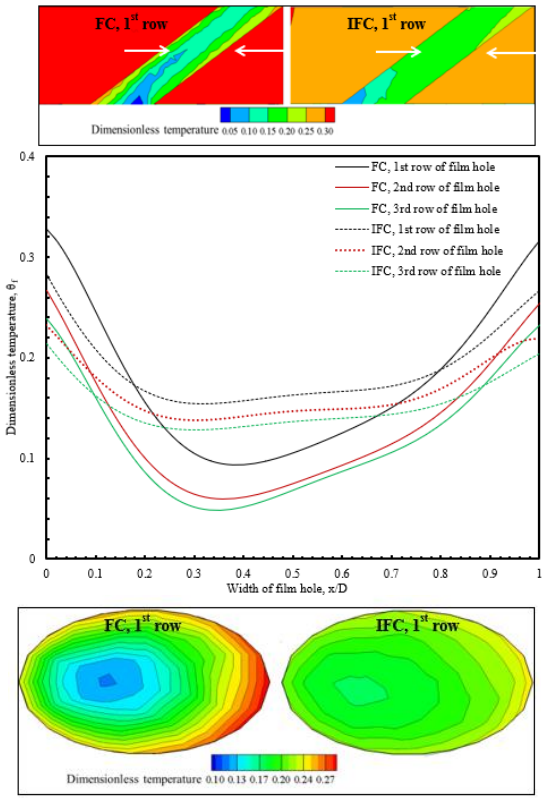

Fig. 12. Dimensionless temperature in the film hole for FC and IFC at mid height.

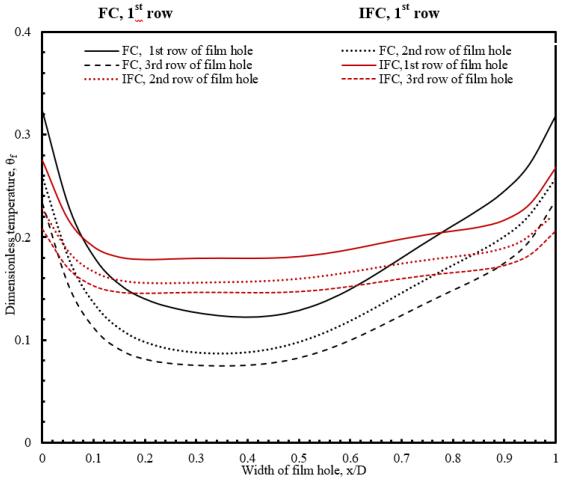

Fig. 13. Dimensionless temperature in the film hole for FC and IFC at exit.

In Fig. 14, the dimensionless temperature is depicted along the film hole's upstream (AA') and downstream (BB') sides. Generally, the dimensionless wall temperature on the

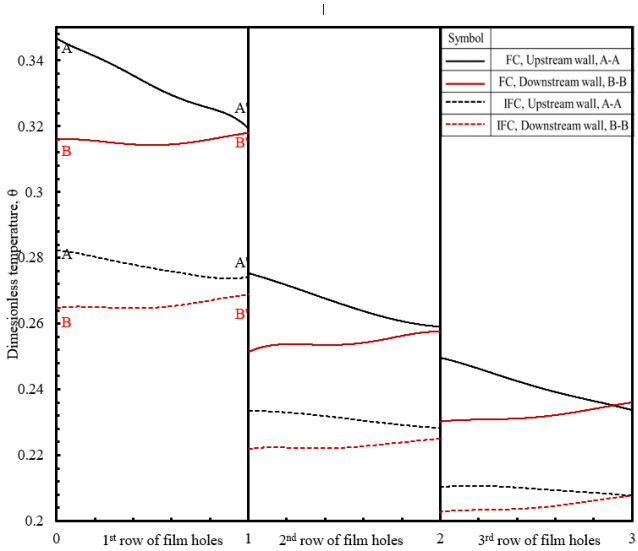

Fig. 14. Dimensionless temperature variation along the film hole wall.

upstream side (AA') is higher than on the downstream side (BB'). The temperature value along line AA' continuously reduces for both FC and IFC cases. But the temperature values for FC (0.34 to 0.32) are higher than IFC (0.28 to 0.27) case. The temperature difference between the inlet (A) and exit (A') of the film hole is also higher for the FC case. Along line BB', the temperature values remain more or less constant for both FC and IFC cases. The FC case exhibits a higher temperature (~0.32) than the IFC (~0.26). The temperature variation along the length of the film hole (AA' and BB') in the down stream rows 2 and 3 is the same as it was in the first row of the film hole. Yet, as compared to the upstream rows, the temperature value continuously decreases in the downstream rows. In the rows downstream of the film hole, it is seen that the temperature difference between the lines AA' and BB steadily decreases.

3.2.2 Downstream of Film Hole

The difference in film coverage above the area of interaction between configurations of FC and IFC is explained by plotting dimensionless temperature along the vertical lines L11, L21, and L31, refer to Fig. 15. Due to the jet lift off the mainstream Fluid entrains between the film jet and the interaction wall, thereby film temperature rises near the wall. For the FC configuration, the temperature pattern along line L11 shows a peak at z/D ~ 0.6. This represents the entrained fluid temperature. The temperature then reduces up to z/D ~ 1.4, corresponding to the coolant jet position (refer to inset in Fig. 15). Thereafter, temperature continuously increases up to the mainstream (z/D ~ 2.4), where the dimensionless temperature value becomes unity. On the other hand, in the IFC case, the temperature variation in the film is comparatively uniform. The temperature on the wall (z/d = 0) is lower for the IFC compared to the FC case. Temperature values up to z/D ~ 1.2 remain almost constant and then increase to the mainstream temperature (z/D ~ 2.4). The uniform temperature distribution within the film may be attributed to the film hole exit profile.

In zones 3 and 4, along lines L21 and L31, the fluctuation and magnitude of temperature are comparatively lower than the upstream row of film holes. It is interesting to notice that the mainstream.

Position shifts upward in the downstream rows due to the presence of carried-over film from the upstream row. The film height is more for the FC case, as seen from the insets in Fig. 15.

3.2.3 Nusselt Number Variation

Figure 16 shows the Nusselt number along the film hole's upstream (AA') and downstream (BB') sides. For FC configuration, the Nusselt number continuously increases along the film hole's length (inlet, A to exit, A'). For the IFC case, the Nusselt number decreases along line AA. The Nusselt number range for the IFC case is high (~230 to 80) as compared to FC (~50 to 90). In the downstream side (i.e., BB), for the FC case, the Nusselt number value continuously decreases with a magnitude range of about 90 to 40. But for IFC, the Nusselt number increases from inlet (~50) up to mid-length (~75) and then decreases till the exit (~55) of the film hole. In the downstream rows of film holes 2 and 3, the Nusselt number distribution for both FC and IFC remains more or less the same as in the case of 1st row of the film hole.

3.3 Interaction Surface

3.3.1 Heat Flux Variation

Figure 17 displays the changes in the non-dimensional surface heat flow at the contact surface along line ab.The values of the heat flux decrease in a consistent manner when moving downstream from zone 1 to zone 4 for either the FC or the IFC configuration. In zone 1, where x/d is equal to 0, the non-dimensional local heat flow reaches its maximum value of unity near the upstream end of the plate; see Fig.17 for more information. After a given distance from the upstream end of the plate, the heat flux drops off dramatically, and then it continues to drop off gradually until it is almost at the first row of film

holes. The behavior of the local heat flux is virtually identical for both the FC configuration and the IFC configuration; however, the IFC instance exhibits a considerably larger value. As the flow approaches the film holes first row, the film coolant jet's presence causes the heat

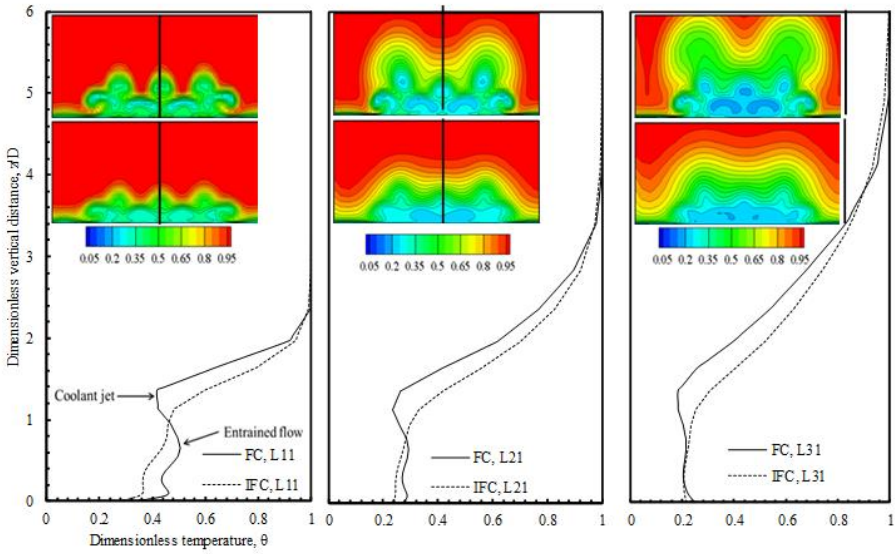

Fig. 15. Dimensionless temperature variation along vertical direction for FC and IFC at L11, L21, and L31.

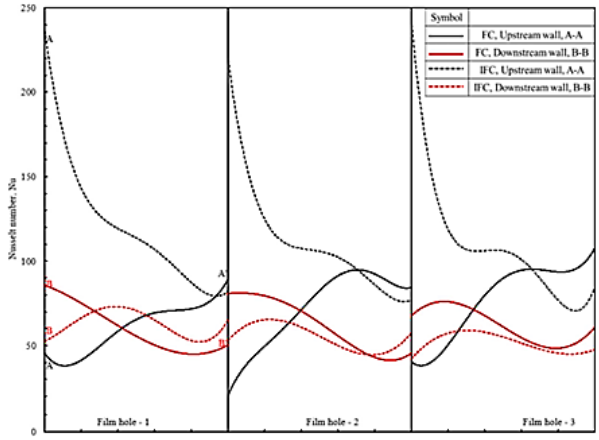

Fig. 16. Nusselt number variation along the film hole wall.

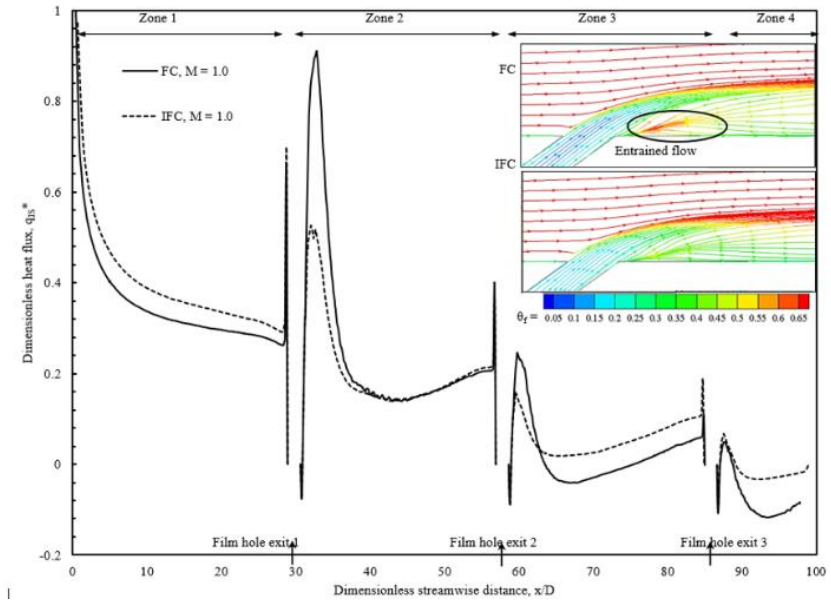

Fig. 17. Dimensionless heat flux distribution on the interaction surface along line ab for FC and IFC case.

flux to rise quickly. This becomes clear as the flow approaches the film holes first row. At the leading edge of the film hole, however, the heat flux diminishes until it is equal to zero.

The values of the heat flux are seen to be negative in the region positioned downstream of the edge of the first row of trailing film holes. Conduction action within the solid plate moving in the direction of the steam is what is responsible for this reversed heat flux direction from the plate to the film. This effect is due to the fact that the plate is heated from the bottom up. The temperature of the plate rises as a result of rapid degradation of the film cooling along the streamwise direction, and heat is transferred from the downstream region to the upstream region. As a direct result of this, the temperature of the plate rises to a level that is higher than the temperature of the film located directly above it, and the direction of the heat flux is altered. Heidmann *et al.* (2010) made SIMILAR observations that are very similar to ours. The mainstream Fluid becomes entrained beneath the coolant jet that is pulled off the plate further downstream of the film hole. This entrained flow causes the film temperature to increase closer to the wall, as was indicated earlier. As a consequence, the value of the heat flux shoots up to a much higher level (peak). The separated film jet is reattached to the surface as a result of the overhead mainstream flow, which causes it to bend downward. The reattachment point is the name given to this particular site. The reattachment is defined by the complete mixing of the film and the entrained Fluid through the counter-rotating vortex pair; this reduces the overall film temperature near the wall. As a result, the heat flow falls following the peak all the way downstream to a distance equivalent to approximately seven film hole diameters, as shown in Figure 17. In both the FC and IFC cases, there is hardly any difference in the heat flux variation.

But, at the peak, the heat flux value corresponding to the FC case (~0.9) is much larger than the IFC case (~0.5). This variation is due to the difference in film temperature between FC and IFC cases); also discussed in the previous section. At the reattachment point, both FC and IFC cases exhibit similar values. The heat flux value downstream of the reattachment point remains almost constant until the flow reaches the second row of holes, when the heat flux valley and peak are once again apparent on the upstream and downstream side of the film holes.

The pattern of heat flux variation in zones 3 and 4 is nearly identical to that seen in zone 2. However, the downstream zones' heat flux values are steadily declining. The reattachment point shifts close to the film hole compared to zone 2. The magnitude of the local heat flux peak is highest for the 1st row, followed by the 2nd and 3rd row of film holes; refer to Fig. 17. The peak values corresponding to the FC case are always higher than the IFC case. However, in zone 3 and 4, the heat flux value at the reattachment point and downstream of it is higher for IFC than in the FC case. It is observed that the heat flux values are either zero

or negative beyond x/d > ~ 88 for both FC and IFC cases. On average 4% increased heat flux is observed for FC configuration compared to IFC.

3.3.2 Effectiveness variation

Figure 18 displays the streamwise effectiveness distributions for FC and IFC configurations along line ab on the interaction surface. As originally noted by Colban *et al.* (2007), the overall tendency of effectiveness increases with the downstream distance. In zone 1, the effectiveness rating for both setups constantly grows to the first row of film holes. There is a sudden increase in effectiveness very close to the film hole exit. Downstream of the film hole, the jet lifts off, leading to a rise in the film temperature. The higher film temperature, in turn, reduces the effectiveness value in the immediate downstream of the hole. The detached jet again attaches to the wall. Thus, after the initial decreasing trend, the effectiveness shows a continuous increase up to the 2nd row of film holes. In zone 3, the effectiveness value is higher compared to zone 2. This is due to the fact that the mainstream hinders the transverse mixing of momentum and energy in zone 2, but in zone 3, the mixing is hindered by the film layer. However, the overall pattern of effectiveness distribution in zone 3 is similar to that in zone 2. In zone 4, unlike previous zones, the effectiveness value decreases continuously with increasing distance downstream due to the absence of a downstream film hole.

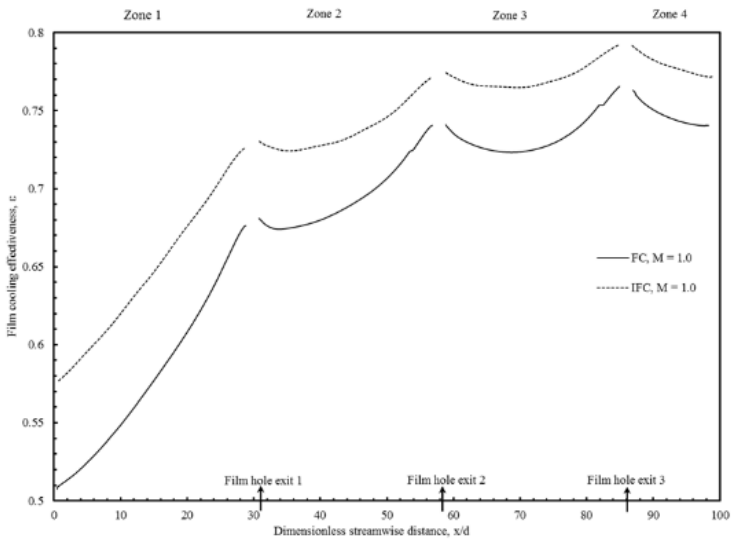

Fig. 18. Film cooling effectiveness on the interaction surface along line ab for FC and IFC case.

The effectiveness values are always higher for the IFC case than the FC, all along the plate length. This is because of the increased impingement heat transfer on the target surface (TS) throughout all zones (discussed in an earlier section). The effectiveness distributions in zones 2, 3, and 4 additionally depend on the film coverage pattern, which is influenced by the film hole exit condition and the coolant-mainstream interaction. Thus, the difference in effectiveness between FC and IFC configurations can be attributed to I the differences in Nusselt number distribution at the target surface and (ii) the flow structure and temperature profile at the exit of the film hole, which depends on the flow field in the coolant chamber and within the film hole.

3.3.3 Nusselt Number Variation

The Nusselt number variation along line *ab* is shown in Fig. 19. The Nusselt number indicates the amount of heat transferred from the Fluid to the wall. Flow in zone 1 up to the distance (x/d ≤22) where the effect of a film hole cannot be felt is comparable to the flow over a flat plate case. Thus, the computed Nusselt number values are plotted against the calculated distribution using the Colban *et al.* (2007) analogy relation for turbulent flow over a flat plate; the comparison is good.

In zone 1, the Nusselt number continuously reduces due to the formation of the thermal boundary layer on the surface from the upstream end of the plate till near the leading edge of 1st row of film holes. A maximum Nusselt number value of 680 is observed at the upstream end of the plate. The Nusselt number distribution remains almost the same in zone 1 between FC and IFC cases, with a marginally higher value for the IFC case. At the upstream of the leading edge of the film hole, the Nusselt number increases to a value of 480 and drops down to 170 at the hole's leading edge. Clearly, this abrupt increase and decrease is the result of the interaction between the mainstream and cooling fluids from the film hole. Similar peaks are observed in the downstream rows of film holes too, but with lower magnitudes. The Nusselt number in zone 1 is higher compared to downstream zones (zones 2 to 4); this reveals the advantage of film cooling. From zone 2 to 4, the Nusselt number reduces progressively (in zones 2 to 4, the heat transfer by analogy is higher by 20% in zone 2, 25% in zone 3, and 27% in zone 4) due to the continuous increase in convective resistance offered by the film coverage. The Nusselt number variations closely follow the trend of heat flux distributions, and the reasons discussed are also valid in this case. Corresponding to the negative heat flux location, the negative Nusselt number is avoided by using the factor' ϕ'. The factor (ϕ) alters its sign in accordance with the direction of heat flux. The peak in Nusselt number formed downstream of film holes due to lift-off phenomena are significantly different between FC and IFC, here FC case exhibits a higher ($\Delta Nu_{P\text{-}Z2} = Nu_{P\text{-}Z2\text{-}FC} - Nu_{P\text{-}Z\ 2\text{-}IFC} = 260$) peak value than IFC. The Nusselt number value corresponding to the peak is 540 and 280 for FC and IFC cases, respectively. Nusselt number value gradually reduces up to the reattachment point from the peak and slowly increases till the upstream end of the next row.

The Nusselt number difference at the peak in zones 3 ($\Delta Nu_{P\text{-}Z3} = 60$) and 4 ($\Delta Nu_{P\text{-}Z4} = 10$) are lower compared to those in zone 2. On the other hand, downstream of the reattachment point, i.e., at the middle of the zone, the difference in Nusselt number value is low in zone 2 ($\Delta Nu_{M\text{-}Z2} = 10$) and progressively increases with the downstream zones 3 and 4 ($\Delta Nu_{M\text{-}Z3} = 20$; $\Delta Nu_{M\text{-}Z4} = 40$). The maximum Nusselt number shows 52% higher values in the FC case.

4. CONCLUSIONS

In this research, a comprehensive comparison is made between film cooling (FC) and combined impingement and film cooling (IFC). The present investigation yields the following conclusions.

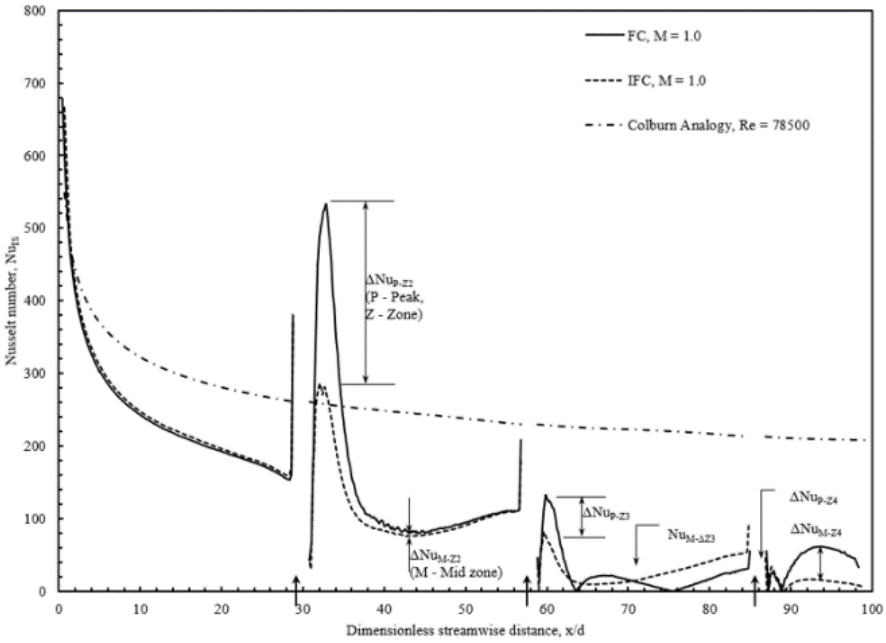

Fig. 19. Nusselt number distribution along streamwise distance for FC and IFC.

- On the target surface, multiple peaks and valleys in heat flux and Nusselt number distribution are observed for the IFC case. In contrast, for the FC case, these values are substantially lower and uniform on the surface. The average Nusselt number shows a 200% increase for IFC configuration compared to FC configuration.
- The dimensionless temperature is lower for IFC than the FC case throughout the surface, even though the distribution remains the same. However, the peak temperature shows variations of 17.3% between the two.
- The dimensionless temperature values for the film hole exit are higher for the FC case. However, it is more uniform for IFC cases in the 30 to 80% range from the leading edge.
- The heat flux and Nusselt number values on the upstream wall of the film hole are higher for IFC than FC, but on the downstream wall, the values are of a similar range.
- FC configuration wall shows consistently higher temperatures than the IFC configuration wall.
- On the interaction surface, a 4% increased heat flux is observed for FC compared to the IFC configuration.
- Nusselt number values on the interaction surface are higher for FC than IFC. The maximum Nusselt number shows 52% higher values in the FC case.
- Although the variation of film cooling effectiveness in the streamwise direction follows the same trend for both FC and IFC, the IFC case shows a 4.6 % increase in average effectiveness values.

ACKNOWLEDGEMENT

This work is carried out under the guidance of late Prof. B V S S S Prasad. The authors are grateful to him for his help and guidance.

REFERENCES

Babu, S. and S. Anish (2020). Computational predictions of velocity ratio and ejection angle on purge flow in a linear turbine cascade with upstream disturbance. *Journal of Applied Fluid Mechanics*13 (1), 335-347. https://doi.org/10.29252/jafm.13.01.29942

Colban, W., K. A. Thole and M. Haendler (2007). Experimental and computational comparisons of fan-shaped film cooling on a turbine vane surface. *ASME-Journal of Turbomachinery* 129, 23-31

Ekkad, S. V., Y. Huang and J. C. Han (1999). Impingement heat transfer on a target plate with film cooling holes. *AIAA-Journal of Thermophysics and Heat Transfer* 13(4), 522-528.

Fu, J., Y. Cao, C. Zhang, and J. Zhu (2020). Investigation of the conjugate heat transfer and flow field for a flat plate with combined film and impingement cooling. *Journal of Thermal Science* 29(4), 955-971.

Hollworth, B. R. and L. Dagan (1980). Arrays of impinging jets with spent fluid removal through vent holes on the target surface-part 1: average heat transfer. *Journal of Engineering and Power* 102 (4), 994-999.

Heidmann, J. D., A. J. Kassab, E. A. Divo, F. Rodriguez and E. Steinthorsson (2010). Conjugate heat transfer effects on a realistic film-cooled turbine vane. In *ASME Turbo Expo*, GT2003-38553, Atlanta, Georgia, USA.

Jingzhou, Z., X. Haoa and Y. Chengfeng (2009). Numerical study of flow and heat transfer characteristics of impingement/effusion cooling. *Chinese Journal of Aeronautics* 22, 343-348.

Jiang, Y. T., H. F. Deng, X. L. You, H. J. Zhao and G. Q. Yue (2021). Numerical investigation on film cooling mechanism with different coolant delivery configurations. *Journal of Applied Fluid Mechanics* 14(1), 175-185.

Jung, Y. E., D. H. Lee, S. H. Oh, K. M. Kim and H. H. Cho (2010, June). Total cooling effectiveness on a staggered full-coverage film cooling plate with impinging jet. In *ASME-Turbo Expo 2010*, GT2010-23725, Glasgow, U.K.

Katti, V. and Prabhu, S. V. (2008). Heat transfer enhancement on a flat surface with axisymmetric detached ribs by normal impingement of circular air jet. *International Journal of Heat and Fluid Flow* 29(5), 1279-1294.

Metzger, D. E. and R. S. Bunker (1990). Local heat transfer in internally cooled turbine airfoil leading edge regions: part ii—impingement cooling with film coolant extraction. *ASME - Journal of Turbomachinery* 112 (3), 459-466.

Miao, J. M. and C. Y. Wu (2006). Numerical approach to hole shape effect on film cooling effectiveness over flat plate including internal impingement cooling chamber. *International Journal of Heat and Mass Transfer* 49, 919-938.

Oh, S. H., D. H. Lee, K. M. Kim, M. Y. Kim and H. H. Cho (2008, June). Enhanced cooling effectiveness in full-coverage film cooling system with impingement jets. In *ASME-Turbo Expo 2008*, GT2008-50784, Berlin, Germany.

Ravelli, S., L. Dobrowolski and D. G. Bogard (2010, June). Evaluating the effects of internal impingement cooling on a film cooled turbine blade leading edge. In *ASME Turbo Expo 2010,* Paper id: GT2010-23002, Glasgow, UK.

Rhee, D. H., J. H. Choi and H. H. Cho (2003). Flow and heat (mass) transfer characteristics in an impingement/effusion cooling system with cross-flow. *ASME - Journal of Turbomachinery*125, 74-82.

Raj, D. P. (2013). Numerical heat transfer analysis of a flat plate using combined jet impingement and film cooling, with flow patterns. *IJTRT* 2(11), November 2013, 2078-2086.

Zhang, C. and Z. Wang (2019). Influence of streamwise position of crescent-shaped block on flat-plate film cooling characteristics. *Journal of the Brazilian Society of Mechanical Sciences and Engineering* 41(11), 1-14.

Zhang, W. and H. R. Zhu (2021). Film Cooling performance of the staggered arrangement of auxiliary holes and main holes on a flat plate. *Journal of Applied Fluid Mechanics* 14(3), 741-752.